Helically Twisted Microstructured Polymer Optical Fiber and Its Application as a Torsion and Strain Sensor

João Preizal , *Member, IEEE*, Lúcia Bilro , Rogério Nogueira , *Member, IEEE*, and Ricardo Oliveira

Abstract—In this letter, we report for the first time the fabrication and sensor application of a helically twisted poly-methylmethacrylate (PMMA) microstructured polymer optical fiber (mPOF). The fabrication was done by mechanically twisting the mPOF while passing it through a miniaturized Peltier element. The structure was created with a helical pitch of $\sim$700 μm, producing a series of spectral dips at the low loss region of PMMA, namely at the 400 to 500 nm region. The structure has been characterized to torsion showing that it can sense the twist direction with high sensitivities (48–53 nm/(rad/mm)). The strain sensor application has also been demonstrated, showing a negative sensitivity response with absolute values of 0.8–0.9 pm/$\mu\varepsilon$. The soft and stretchable nature of mPOFs combined with helical structures will provide new opportunities for the development of highly tunable filters and innovative smart sensors.

I. INTRODUCTION

HELICALLY twisted optical fibers (HTOF) have been a hot topic due to their interesting telecom and sensor applications. Examples of the former include the capability to generate orbital angular momentum (OAM) [1], the suppression of high-order laser modes [2], the capability to manipulate the loss and polarization state of light [3], and the possibility to use them as fiber couplers [4], [5] and sensors. Concerning the latter, it is possible to mention the capability to measure common parameters as it occurs in standard optical fiber structures, as is the case of strain [6], [7] and temperature [7], but it can also be used to measure other parameters such as torsion [7], transverse-load [7], curvature [8] and electric current [9].

Heat deforming an optical fiber in a helical shape permanently imposes a helical twist along its length. This has been done by heating the fibers to their softening temperature, through a CO_2 laser [10], electric arc [11], hydrogen-oxygen flame [12], and in an oven [13]. HTOFs have been reported using glass optical fibers (GOFs) with noncircular symmetry cross section [10], and with single- and double-helix symmetry [14]. However, the use of silica microstructured optical fibers, also known as photonic crystal fibers (PCFs), has been one of the most reported [1], [2], [7], [15], due to their attractive characteristics. Twisting PCFs forces the pointing vector of the cladding-guided light to follow a spiral shape into the azimuthal space. This allows the core mode to phase-match leaky cladding modes at specific wavelength regions, leading to sharp spectral resonances in the transmission spectrum.

In 2012, Xu et al. [16] proposed for the first time, a helically twisted polymer optical fiber (POF) owing to the promising features of polymers. Unfortunately, this structure has never been reported in the literature, probably due to the popularity of GOFs. Despite being of similar age, POFs have been overwhelmed by the popularity of GOFs. This is mainly due to the higher transparency of GOFs. However, POFs have been used for short and medium distances such as in industrial, automotive, or home networking. Furthermore, they are more flexible, non-brittle, easier to functionalize, biocompatible, and have higher thermo-optic coefficients. It is also possible to highlight its lower Young's modulus (i.e., 1.8–3.1 GPa vs. 70 GPa), higher elastic limits ($\sim$5% vs <1%), and low processing temperatures (i.e., $\sim$100 °C vs. $\sim$1200 °C), which helps its production and also its post-processing. Also, the possibility to use technologies such as drilling [17], preform casting [18], and 3D printing [19], allows an easier implementation of microstructured designs, when compared to glass. This is especially relevant in POFs since the achievement of single-mode (SM) behavior with step-index profiles is difficult to reach due to doping diffusion. The advent of microstructured designs, not only simplifies the fabrication process but also allows the easy achievement of SM behavior at the low-loss region of polymers.

Thanks to the interesting properties of POFs, they could play an important role in the fabrication of flexible smart sensors as was already explored in a variety of fiber optic devices developed with the well-known fiber Bragg grating (FBG) technology [20]. The fabrication of these spectral filters is normally done through the phase mask technique, where a photosensitive
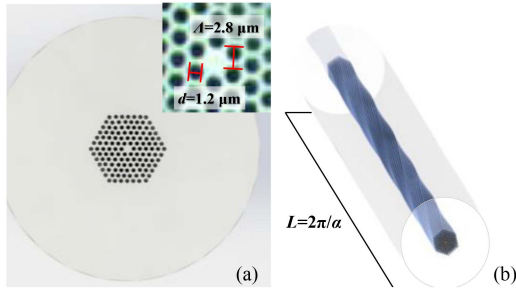
Fig. 1.   Schematic of the mPOF (a) transversal cross-section (the inset shows the microscope image with the corresponding dimensions) and (b) longitudinal section after one twisting period ($L = 2\pi/\alpha$).

POF is exposed to a periodic ultraviolet (UV) pattern, allowing the modulation of its refractive index. The use of photosensitive materials, UV lasers, and phase masks, makes the process complex and costly. Furthermore, drawbacks associated with long-term stability have been reported, owing to the thermal and stress relaxation of the polymer chains [21], [22]. Therefore, it is a strong motivation for the study of other novel structures capable of suppressing these issues.

In HTOF, the permanent helical twist is done at the soft temperature of the material that composes the fiber. After cooling down, the helical structure is permanently engraved in the fiber, making it very robust [23]. Owing to the special properties of POFs and HTOFs, the study of the symbiotic effect between these two structures is remarkably interesting. Like GOFs, POFs can also be post-processed with a permanent twist. Additionally, the melting point of polymer materials is much lower than that of silica, so the requirement of high-power heat sources is not needed and the use of simpler heating elements can be used, making the fabrication much easier.

In this letter, we describe for the first time, to the best of our knowledge, the fabrication and sensor application, either as torsion and strain, of a helically twisted polymethylmethacrylate (PMMA) microstructured polymer optical fiber (mPOF). The structure is created through a dedicated setup that allows the twisting of the fiber while passing it through a miniaturized heat source, namely a thermoelectric cooler (TEC) module, which is cheaper and simpler than conventional heat sources used to produce HTOFs in GOFs. This allows to permanently twist the mPOF in a helical shape. This originated a series of spectral resonances at the low loss region of the fiber, namely at the visible region (500-800 nm). The newly formed structure will be characterized to torsion and strain, and the results will be compared with the literature regarding similar structures produced in PCFs.

A. Theory

The POF used in this work was a PMMA mPOF, purchased from Kyriama Pty. It is composed of 6 layers of air holes hexagonally organized in the cladding region, and one missing central hole, as shown in Fig. 1(a). This fiber has an attenuation of $\approx$3.8 dB/m at the wavelength region between 500 and 700 nm.

The air holes of the mPOF have a diameter of $d \approx 1.2 \ \mu$m and a hole spacing of $\Lambda \approx 2.8 \ \mu$m allowing the fiber to be the endlessly single mode ($d/\Lambda = 0.43$) [24]. When we induce a gentle twisting

force ($\alpha\Lambda \ll 1$, where α is the twist rate on the mPOF, the air holes will be twisted along the central axis of the fiber, leaving a periodic pattern as exemplified in Fig. 1(b). Cladding light propagating in this helical lattice of hollow channels is forced to follow a spiral path, diverting a fraction of the axial momentum flow into the azimuthal direction [1]. The fundamental core mode phase matches these cladding modes creating a series of dips in the transmission spectrum. According to reference [1], the resonant wavelength, λ_R, of the HTOF, can be described as:

$$\lambda_R = 2\pi n_{SM}\rho^2\alpha/l \tag{1}$$

where n_{SM} is the refractive index of the space-filling mode, ρ is the radius of the cladding mode resonance and l is an integer representing its order. Since n_{SM}, ρ, and l are constants, as described experimentally [1], λ_R depends only on α. One important thing to notice in (1) is that the resonant wavelengths scale with the reciprocal of L, ($L = 2\pi/\alpha$). This is different from the phenomenon observed in fiber gratings, where resonant wavelength would scale with L [1]. This proportional relation shows that subjecting the HTOF to external forces such as torsion, α_M, or longitudinal strain, ε, can change the twist rate and thus, cause a wavelength shift. This shift can be estimated by differentiating (1), which gives:

$$\Delta\lambda_R = \lambda_{R0} \left(\frac{\Delta n_{SM}}{n_{SM0}} + \frac{\Delta\alpha}{\alpha_0} + \frac{2\Delta\rho}{\rho_0} \right) \tag{2}$$

being n_{SM0}, ρ_0, and α_0 the values when the fibers are without any external load. This equation can be further developed allowing to reach [6]:

$$\frac{\Delta\lambda_R}{\lambda_{R0}} = \left(\frac{\alpha_M}{\alpha_0} - \varepsilon \right) - 2\upsilon\varepsilon + \varepsilon\frac{n_{SM0}^2}{2} \left[\upsilon\left(p_{11} + p_{12}\right) - p_{12} \right] \tag{3}$$

where υ defines de Poisson ration and p_{ij}, the photoelastic coefficients. As observed from (3), $\Delta\lambda_R$ is proportional to λ_{R0}, thus, for the sake of better sensitivities, it would be beneficial to work at longer wavelengths. Unfortunately, the attenuation of POFs restricts their use at the visible spectral region, making them unable to scale the sensitivity by working at longer wavelengths.

II. Materials and Methods

A. HTOF Production

To permanently induce a helical twist in the mPOF, the fiber was heated to its softening point (115 °C), through a dual-stage thermoelectric cooler (TEC) module (TECD2, Thorlabs), which was controlled through a temperature controller (model 3040, Newport). To evenly distribute the temperature around the mPOF, we used a 10×10 mm length custom-made brass part (containing a 0.8 mm diameter through hole). This part sits on top of the TEC area (10×12 mm) and allows to transfer the heat generated by the TEC to $\sim$10 mm length of the mPOF. Due to the temperature dissipation at the edges of the brass element, it is expected a Gaussian temperature distribution with a maximum temperature at the center of the brass structure and minima at the edges. A schematic and an infrared photo of this part is shown on the inset of Fig. 2. The experimental setup was composed of three linear translation stages and one rotation stage, all from Newport.
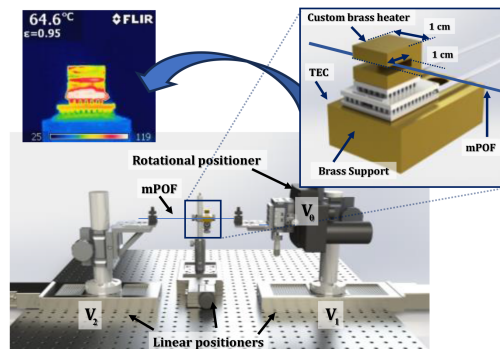
Fig. 2. Schematic of the experimental setup, composed of three linear translation stages, one rotational stage, and the heating element. The inset shows the heating stage composed of brass support, TEC, and a custom brass heater element.

Fig. 3. Experimental setup used for the torsion and strain characterization of the HTOF.

The positioners are connected to a motion controller unit and are computer controlled. A schematic of the implemented setup is shown in Fig. 2.

As seen from Fig. 2, the TEC moves solidary with the central linear stage, which function is to position the heat source in the vicinity of the mPOF. To twist the mPOF, one of its terminals is kept fixed, while the other is solidary with the rotational stage, and spins in the clockwise (CW) direction at a constant velocity, V_θ. This positioner is synchronized with right and left linear stages, which move each of the mPOF terminals in the same direction at V_1 and V_2 speeds, respectively. This allows the longitudinal translation of the mPOF over the heat region, throughout the twisting process. The twist rate in which the fiber is permanently deformed in a helical shape is given by the ratio between the angular and linear velocities of the positioners, such that, $\alpha = V_\theta/V_1$, where $V_\theta = 2\pi/T_\Lambda$, and $V_1 = L/T_\Lambda$, being T_Λ, the heating time per twist period, needed to soften the PMMA material. The values reported in literature for the twist rate in PCFs, ranged between 9.0 and 18.4 rad/mm [1], [25]. According to (1), λ_R is proportional to α, and thus lower resonant wavelengths are expected to be observable for higher twist rates. Taking into account the similarities between the fiber presented in [1] and the one shown in this work, and knowing that the low loss transmission window of the mPOF is located at the visible spectral region, it is a good starting point to use low twist values. In our work, we set $\alpha = 9.7$ rad/mm, corresponding to theoretical twist period, $L = 2\pi/\alpha \approx 650 \ \mu m$. Considering $T_\Lambda = 0.8$ s, this gave $V_\theta = 7.85$ rad/s and $V_1 = 0.81$ mm/s. It is worth mentioning that V_2 was 1% more than V_1 to maintain the fiber under tension during the twisting process. Furthermore, it was considered a total of one hundred periods, to allow sharper resonance dips in the transmission spectrum.

B. Torsion and Strain Test

After the fabrication of the HTOF, we decide to verify its capabilities as a torsion and strain sensor. For that, one terminal of the helically twisted mPOF was glued on top of a v-groove fiber holder, and secured on a 3-axis micrometer translation stage (MBT616D/M, Thorlabs), while the other fiber terminal was secured on a precision fiber rotator (HFR007, Thorlabs),
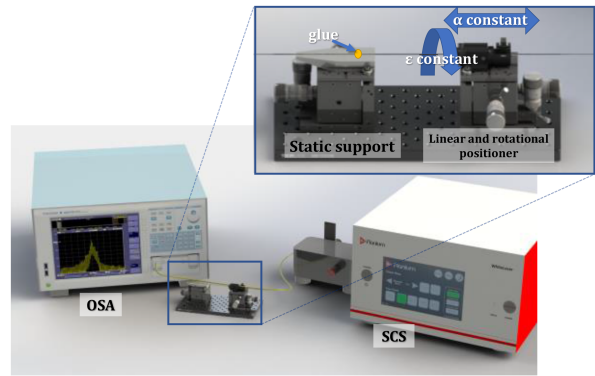
placed on top of another 3-axis translation stage. The distance between the fiber fixed points was ~88.6 mm. The fiber rotator was twisted in steps of 0.0059 rad/mm for the torsion characterization. This characterization was made in the clockwise (CW) and counterclockwise (CCW) directions and the spectra were acquired at each torsion step (13 steps for each direction). Later on, a strain test was also performed with the same setup. For that, one side of the HTOF was kept fixed and the other was pushed through the 3-axis translation stage (i.e., using the micrometer parallel to the fiber). The strain steps were 250 $\mu\varepsilon$ and the spectra were taken for each strain step, in a total of 13 steps. The setup used for the torsion and strain characterization is shown in the inset of Fig. 3.

It is important to note that characterizations were done at stabilized room temperature, allowing to avoid cross-sensitivity issues related to temperature.

To spectrally characterize the polymer HTOF, light from a supercontinuum source (SCS) (WL-SC400-2, Fianium), was coupled to the mPOF through a mechanical splice made with a UV-photosensitive resin. This connection is robust since the mechanical characteristics of the resin (NOA 86H, from Norland), are similar to the ones of the POF. On the opposite side, the mPOF terminal was inserted in a 127 μm bore ferrule connector and connected to the Vis-NIR optical spectrum analyzer (OSA) (AQ6373B, Yokogawa).

III. RESULTS

A. HTOF Characterization

To perform a visual inspection of the changes induced on the mPOF after the post-processing, we visualized the raw and post-processed mPOF samples under a microscope. The images are shown in the top and bottom parts of Fig. 4(a). As seen in those images, the air holes that form the microstructured region of the mPOF (found at the central region of the fiber), run straight along the length of the raw-mPOF. However, a periodic pattern of ~116 μm was observed on the twisted mPOF. Considering the six-fold symmetry of the mPOF, i.e., the air hole structure repeats at every 60° rotation, due to the hexagonal air hole pattern, then, the observed periodic pattern corresponds to only to 1/6 of a full turn. the air hole structure repeats at every 60° rotation, due
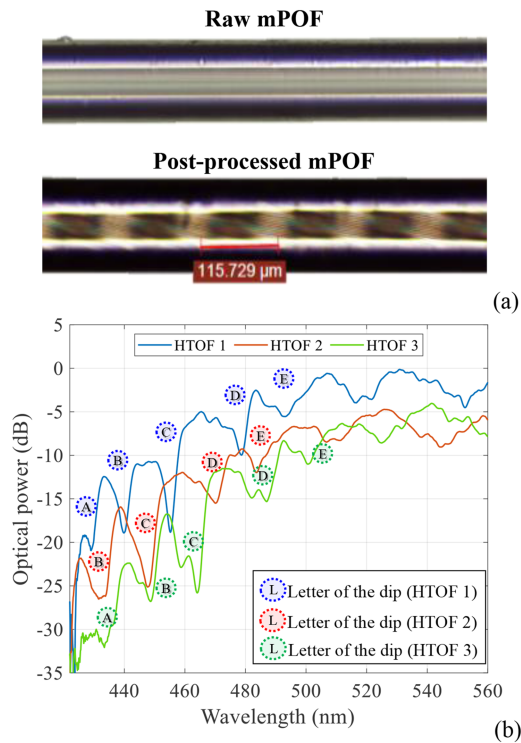
Raw mPOF

Post-processed mPOF

115.729 µm

(a)

(b)

Fig. 4. (a) Microscope images of HTOF 1 untwisted (top), and after inducing a theoretical permanent twist of ∼9.7 rad/mm (bottom), corresponding to an experimental helical twist of 9.0 rad/mm. (b) Spectra of three mPOF samples helically twisted with ∼9.7 rad/mm, showing a series of spectral resonances, as indicated by the ordered letters.

TABLE I
APPROXIMATE RESONANT WAVELENGTHS OF HTOFS

HTOF sample	α (rad/mm)	Resonant wavelength order				
		A	B	C	D	E
1	9.0	429 nm	440 nm	455 nm	479 nm	493 nm
2	8.9	-----	432 nm	448 nm	470 nm	484 nm
3	9.1	433 nm	448 nm	464 nm	486 nm	501 nm

dip wavelength observed in Fig. 4(b), (indicated by the ordered numbers), corresponds to the phase matching of the fundamental mode propagating in the central solid core to the fundamental space-filling cladding modes allowed to propagate in the twisted mPOF. The number of excited cladding modes is a characteristic that depends not only on the twist period but also on the mPOF properties. Furthermore, according to (1), the orbital mode order should be proportional to the reciprocal of wavelength at a fixed twist rate [1]. Thus, each dip resonance shown in Fig. 4(b), corresponds to a different mode order.

The twist period of the HTOFs was measured using a microscope and was about ∼704 µm (8.9 rad/mm) and ∼695 µm (9.1 rad/mm), for the HTOF 2 and HTOF 3, respectively. The results obtained in this work are similar to the ones reached in references [1] and [25], which reported twist rates between 9.0 rad/mm and 18.4 rad/mm in a PCF with a similar air hole structure, and showed spectral dips appearing in the visible region. The literature shows that the effective axial refractive index increases quadratically with the radius, ρ, and thus, the light will refract outwards away from the central axis, making the cladding resonances highly leaky. This leads to the appearance of strong dips in the transmission spectrum [25]. As observed from Fig. 4(b), the strength of the dip losses is more pronounced at the lower wavelength region which coincides with the higher effective refractive index region of the core mode. The explanation lies in the high loss of the cladding resonances which also widens the coupling bandwidth, resulting in losses at the out-of-band region. One possible solution to reduce these losses could be done through the reduction of the number of periods, this would reduce the coupling strength, reducing the bandwidth and leading to a decrease of the out-of-band losses.

Unfortunately, we couldn't visualize the near-field images of the excited cladding modes due to the absence of a tunable laser source located at the visible region.

Regarding the repeatability of the process, it can be seen from Fig. 4(b), that the resonance pattern shown in each HTOF spectrum is similar in all the post-processed samples, showing similar wavelength dip separation for each of the three prepared samples. In Table I, it is presented the approximate resonant wavelength values measured for each HTOF produced in this work.

As observed, the location of the spectral resonances is not exactly the same for all the prepared samples. Again, the results are associated with the soft nature of the POF, making the final twist period vary slightly between samples. Furthermore, errors associated with temperature fluctuations, homogeneity of the mPOF along its length, wrong position of the mPOF on the heating platform, and differences in the fiber pre-tension, could also occur and might require further optimization. However, this

to the hexagonal air hole pattern. Then, the observed periodic pattern corresponds to only 1/6 of a full turn. Therefore, the experimental helical pitch is 6 × 116 µm ∼696 µm, corresponding to a twist rate of ∼9.0 rad/mm. This deviates slightly from the one theoretically predicted (∼650 µm). The reason was attributed to the mPOF soft nature, which makes the fiber able to twist in the unheated regions during its post-processing. Therefore, the twist accumulated on the unheated regions will be released after removing the mPOF from the fiber clamps. This will lead to a post-processed fiber with a twist rate smaller than the one predicted, or in other words, with a higher twist period. Despite this, similar twist periods were measured for different post-processed samples, showing that the process is repeatable. Regarding the output spectrum of the HTOF, the results are shown by the blue continuous line in Fig. 4(b).

It is important to notice that attempts to produce smaller twist periods using the same heating area, temperature and mPOF, were unsuccessful since the fiber breaks easily. Thus, for smaller helical periods, it would be necessary to optimize one of those parameters. However, this was out of the scope of this work. Regarding the spectral characterizations, we did the measurement in three post-processed samples. The results are displayed in Fig. 4(b). These show a series of sharp spectral dips (bandwidth ∼2 nm) located at the 440 to 500 nm wavelength region. This coincides with the low-loss transmission window of PMMA material, which forms the raw material of the mPOF used in this work. According to the literature, each
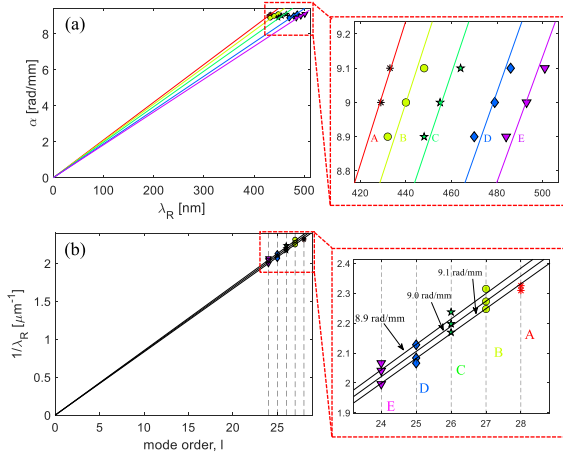
Fig. 5. Twist rate measured from the HTOF samples as a function of the resonant wavelengths A, B, C, D, and E shown in Fig. 4(b). (a) The lines correspond to the linear fits of each resonance, passing through zero wavelength when the twist rate is zero. (b) Reciprocal wavelength as a function of mode order for the experimental results (markers). The continuous lines were plotted using (1) and assuming $n_{SM}\rho^2 = 210\ \mu m^2$.

was out of the scope of this work. Regarding the difference between the spectral attenuation for each of the three samples analysed, we stress that the measurements were carried by fusion splicing a POF to a silica fiber (using UV resin) and by using a ferrule connector to secure the terminal of the mPOF into the OSA. Thus, slight misalignments on those fiber sections can induce losses, and, considering that the fiber is moved from the measurement setup to the fabrication setup and later, again to the characterization setup, it is reasonable to consider some degree of inaccuracy. Despite that, we stress that the noise level in all the spectra is too high, and thus, applications of these spectral filters could only be seen in the sensors field since the measurements are codified in wavelength as we will explore in the next subsections.

Interestingly the data compiled in Table I, allowed to check the influence of the twist rate on the location of the resonant wavelength. This can be visualized in Fig. 5(a).

As observed in Fig. 5(a), the resonant wavelengths A, B, C, D and E, scale linearly with α. According to (1), the orbital mode order, l, is proportional to the reciprocal wavelength at a fixed twist rate, meaning that $l = 0$, when $\lambda_R \to \infty$. Applying this condition to the experimental data shown Fig. 5(a), as already done in [1], and using (1), it allows to obtain the results presented in Fig. 5(b). These show that the resonances A, B, C, D and E displayed in Fig. 4(b) for each of the HTOFs, run from $l = 24$ to $l = 28$. To reach these values we set the product $n_{SM}\rho^2$ equal to $210\ \mu m^2$.

B. Torsion Sensor Characterization

Fig. 6 shows three different spectra obtained for the dips located at 450 nm and 472 nm, regarding three different torsion values imposed to the HTOF (sample 1, shown in Fig. 4(b)), namely without twist (green) and when twisted with $+0.018$ rad/mm in the CW direction (red) and with -0.018 rad/mm in the CCW direction (blue), respectively.
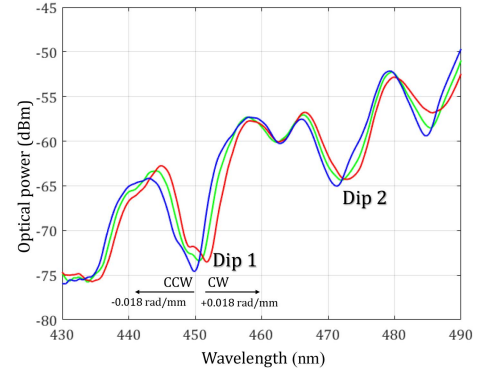

Fig. 6. Spectra wavelength shift observed when the HTOF1 is without twist (green) and when it was twisted at 90°: CW (red), and CCW (blue).

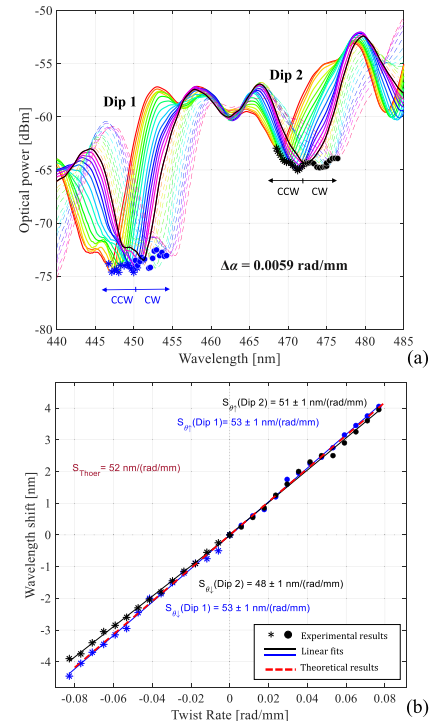Fig. 7. (a) Spectra obtained at different twist rates for the dip wavelengths located at ~450 nm and ~472 nm for the HTOF sample 1 shown in Fig. 4(b), The minimum dip wavelength is indicated by "∗" and "•" markers, for the CCW and CW direction, respectively. (b) Dip wavelength shift as a function of the twist rate for the CCW and CW characterization. On the same graph, it is shown the first-order linear regressions obtained, as well as the theoretical curve (dashed line) obtained from (3).

As observed from Fig. 6, the spectrum is red- and blue-shifted when the HTOF is twisted CW and CCW, respectively. Pure axial torsion changes the twist rate, α, and since λ_R is proportional to α, as described in (3), the observed spectral wavelength shift agrees with the theory. This indicates an interesting characteristic of this structure, namely the capability to measure the twist direction. In Fig. 7(a), we show the spectral results regarding the full torsion characterization. The ones shown with a continuous line are related to the CCW motion, while the dashed ones refer to the CW direction.

As observed from Fig. 7(a), the spectra are linearly blue- and red-shifted when the HTOF is twisted CCW and CW,

respectively. By tracking the central dip wavelength as shown by the "∗" and "•" markers, for the CCW and CW direction, respectively, it was possible to produce the graph shown in Fig. 7(a), which represents the dip wavelength shift as a function of the twist rate. This shows a proportional behavior for each of the analyzed dips and thus, a first-order linear regression model was applied to the experimental data points, for each twist direction. The sensitivities obtained from the absolute value of the slope for the CCW and CW direction were, 62 ± 1 nm/(rad/mm) (CCW) and 51 ± 1 nm/(rad/mm) (CW) for the resonance dip A, while 48 ± 1 nm/(rad/mm) (CCW) and 53 ± 1 nm/(rad/mm) (CW), for resonance dip B. The values were close to each other, being the slight differences probably associated with the detection method used to find the dip wavelength, i.e., center of the mass at 0.5 dB above the minimum. Since the spectral dips slightly change their shape as a function of the twist rate, i.e., mainly due to the non-flat response of the source and due to the absence of normalization, this leads to obtaining errors in the precise location of the dip wavelength. Thus, proper signal normalisation should be performed before the characterization. Analytical results predicted from (3), considering $\varepsilon = 0$ $\mu\varepsilon$, $\lambda_{R0} = 472$ nm and $\alpha_0 = 9.0$ rad/mm, revealed a sensitivity close to the one reached experimentally, namely 52 nm/(rad/mm). The results have been plotted in Fig. 7(b) for comparison, showing good agreement.

Comparing the sensitivity results reached in this work with the ones found in the literature, we found out that they are higher than those reported in [26], which most of the times report sensitivity values on the order of tens or hundreds of pm/(rad/mm). Furthermore, the values reached in this work closely match the ones observed in the literature for the same twisted structures in silica PCF, i.e., ~56 nm/(rad/mm) [6]. However, we stress out that POFs are more flexible, non-brittle, compliant, and offer higher elastic limits [27], [28], meaning that they can extend the limits and range of applications.

C. Strain Sensor Characterization

Fig. 8(a) shows the spectra collected for each strain step during the strain characterization of the HTOF sample one, which is shown in Fig. 4(b).

As seen in Fig. 8(a), the spectra were blue-shifted with increasing strain. Furthermore, the dip wavelengths calculated from the center-of-mass method at 0.5 dB above the minima were also shown with "•" and "∗" markers for the dip D and E resonances, respectively. In Fig. 8(b), we show the associated dip wavelength shifts as a function of applied strain. A linear regression model was applied to the data points, allowing obtaining sensitivities of -0.90 ± 0.04 pm/$\mu\varepsilon$ and -0.84 ± 0.04 pm/$\mu\varepsilon$, for the dip D and E resonances, respectively. The sensitivity results obtained for each of the dips were similar, being within the same range. Comparing these results with the ones reported in [6], it can be seen that the negative wavelength shift response with increasing strain is also in agreement with the literature. Furthermore, the absolute value of the sensitivity reached in this work was similar to the one reported in the literature for twisted PCFs, i.e., -1.18 pm/$\mu\varepsilon$ [6], being the slight differences associated with the lower dip wavelength used in this work,

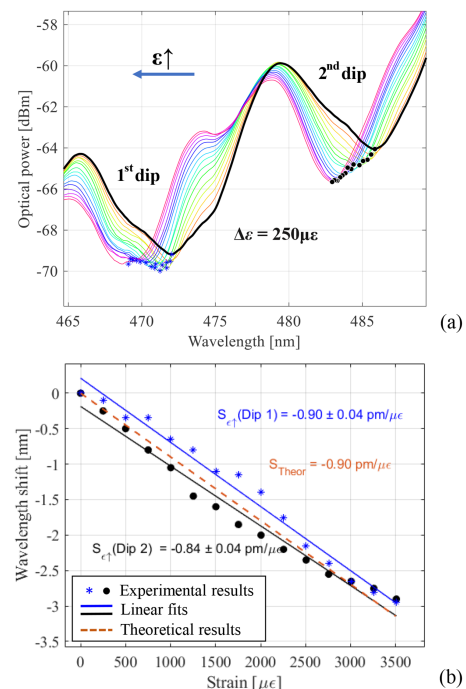Fig. 8. (a) Spectra showing the dip wavelengths located at ~472 nm and ~486 nm, acquired for different strain steps. The minima dip wavelengths are indicated by "∗" and "•" markers for the ~472 nm and ~486 nm, respectively, (b) Corresponding dip wavelength shifts as a function of strain, for the dip D and E. On the same graph, it is shown the first-order linear regressions obtained for each of the data points. The theoretical curve obtained from (3) is plotted with a dashed line.

i.e., 470–485 nm vs. 800 nm. Also, the absolute values of the sensitivities are within the same values reported for polymer fiber Bragg gratings [20]. These results prove that the HTOF can be used for longitudinal strain sensing, giving good prospects regarding the high tunable range associated with the high elastic limits of POFs [27], [28], and their easy fabrication.

Finally, to validate the results, we estimated the strain sensitivity through the analytical calculation, using (3). For this, it was assumed $\lambda_{R0} = 486$ nm, $n_{SM} = 1.49$, $\upsilon = 0.35$, $p_{11} = 0.121$, $p_{12} = 0.270$ [29], and no effect on α_M. This allowed to obtain a sensitivity of -0.90 pm/$\mu\varepsilon$, which closely match the one reached in the experimental results. The theoretical data points were added to Fig. 8(b) for comparison purposes, showing good agreement between experimental and theoretical results.

It is known that the temperature cross-sensitivity can have a detrimental effect in field applications. Thus, its value needs to be taken into account. Considering that the temperature sensitivity is due to the thermo-optic (ξ) and thermal expansion (α) coefficients, which for PMMA fiber are -8.5×10^{-5}/°C [30] and 6×10^{-5}/°C [31] respectively, and considering $\lambda_R = 486$ nm, it results in a temperature sensitivity of $S_T = \lambda_R(\xi + \alpha) \approx -12$ pm/°C, wich is the same in magnitude to that of an HTOF made of silica [7]. Based on this value, we estimate a temperature cross-sensitivity of $\approx -2.3 \times 10^{-4}$ (rad/mm)/°C and ≈ 13 $\mu\varepsilon$/°C, for the torsion and strain, respectively, which can be considered as low, for the majority of the applications.

IV. CONCLUSION

This work showed for the first time to the best of our knowledge, the capability to produce a helically twisted mPOF. The structure showed a series of spectral dips located at the visible region. The low temperatures used to post-process this kind of fiber facilitates their production when compared to their silica counterparts. We also explored the capabilities of the newly formed structure for torsion and strain sensing applications. The results showed that the structure can be used to sense those parameters with high sensitivities and also able to discriminate the twist direction. The high elastic limits of POFs will make this fiber structure very attractive, namely to extend the limits of operation of the commonly used silica fiber sensors. Overall, this work will pave the way for a new class of devices fabricated in POFs, making them very attractive for future fiber optic applications.

REFERENCES

[1] G. K. L. Wong et al., "Excitation of orbital angular momentum resonances in helically twisted photonic crystal Fiber," *Science*, vol. 337, no. 6093, pp. 446–449, 2012, doi: 10.1126/science.1223824.

[2] C. Fu et al., "High-order orbital angular momentum mode generator based on twisted photonic crystal fiber," *Opt. Lett.*, vol. 43, no. 8, 2018, Art. no. 1786, doi: 10.1364/OL.43.001786.

[3] R. Ulrich and A. Simon, "Polarization optics of twisted single-mode fibers," *Appl. Opt.*, vol. 18, no. 13, 1979, Art. no. 2241, doi: 10.1364/AO.18.002241.

[4] U.-C. Paek, Y. Chung, S. Oh, and K. R. Lee, "Fabrication of helical long-period fiber gratings by use of a CO$_2$ laser," *Opt. Lett.*, vol. 29, no. 13, pp. 1464–1466, Jul. 2004, doi: 10.1364/OL.29.001464.

[5] V. M. Churikov, V. I. Kopp, and A. Z. Genack, "Chiral diffraction gratings in twisted microstructured fibers," *Opt. Lett.*, vol. 35, no. 3, pp. 342–344, 2010, doi: 10.1364/OL.35.000342.

[6] X. Xi, G. K. L. Wong, T. Weiss, and P. S. J. Russell, "Measuring mechanical strain and twist using helical photonic crystal fiber," *Opt. Lett.*, vol. 38, no. 24, pp. 5401–5404, 2013, doi: 10.1364/ol.38.005401.

[7] C. Fu et al., "Transverse-load, strain, temperature, and torsion sensors based on a helical photonic crystal fiber," *Opt. Lett.*, vol. 44, no. 8, pp. 1984–1987, 2019, doi: 10.1364/OL.44.001984.

[8] L. Zhang, Y. Liu, X. Cao, and T. Wang, "High sensitivity chiral long-period grating sensors written in the twisted Fiber," *IEEE Sens. J.*, vol. 16, no. 11, pp. 4253–4257, Jun. 2016, doi: 10.1109/JSEN.2016.2542842.

[9] R. Beravat, G. K. L. Wong, X. M. Xi, M. H. Frosz, and P. S. J. Russell, "Current sensing using circularly birefringent twisted solid-core photonic crystal fiber," *Opt. Lett.*, vol. 41, no. 7, pp. 1672–1675, 2016, doi: 10.1364/OL.41.001672.

[10] X. Kong, K. Ren, L. Ren, J. Liang, and H. Ju, "Chiral long-period gratings: Fabrication, highly sensitive torsion sensing, and tunable single-band filtering," *Appl. Opt.*, vol. 56, no. 16, pp. 4702–4707, 2017, doi: 10.1364/AO.56.004702.

[11] J. Li et al., "Sampled Bragg gratings formed in helically twisted fibers and their potential application for the simultaneous measurement of mechanical torsion and temperature," *Opt. Exp.*, vol. 26, no. 10, pp. 12903–12911, 2018, doi: 10.1364/oe.26.012903.

[12] C. Fu et al., "Orbital angular momentum mode converter based on helical long period Fiber grating inscribed by hydrogen–Oxygen flame," *J. Light. Technol.*, vol. 36, no. 9, pp. 1683–1688, May 2018, doi: 10.1109/JLT.2017.2787120.

[13] O. V Ivanov, "Fabrication of long-period fiber gratings by twisting a standard single-mode fiber," *Opt. Lett.*, vol. 30, no. 24, pp. 3290–3292, 2005, doi: 10.1364/ol.30.003290.

[14] V. I. Kopp et al., "Single- and double-helix chiral fiber sensors," *J. Opt. Soc. Amer. B*, vol. 24, no. 10, pp. A48–A52, 2007, doi: 10.1364/JOSAB.24.000A48.

[15] C. Fu, Y. Wang, Z. Bai, S. Liu, Y. Zhang, and Z. Li, "Twist-direction-dependent orbital angular momentum generator based on inflation-assisted helical photonic crystal fiber," *Opt. Lett.*, vol. 44, no. 2, pp. 459–462, 2019, doi: 10.1364/ol.44.000459.

[16] H. X. Xu and L. Yang, "Comparison of chiral and conventional long period Fiber gratings," in *Proc. IEEE Symp. Photon. Optoelectron.*, 2012, pp. 1–4, doi: 10.1109/SOPO.2012.6270903.

[17] M. van Eijkelenborg et al., "Microstructured polymer optical fibre," *Opt. Exp.*, vol. 9, no. 7, pp. 319–327, 2001, doi: 10.1364/OE.9.000319.

[18] Y. Zhang et al., "Casting preforms for microstructured polymer optical fibre fabrication," *Opt. Exp.*, vol. 14, no. 12, pp. 5541–5547, 2006, doi: 10.1364/OE.14.005541.

[19] K. Cook et al., "Air-structured optical fiber drawn from a 3D-printed preform," *Opt. Lett.*, vol. 40, no. 17, pp. 3966–3969, 2015, doi: 10.1364/ol.40.003966.

[20] R. Oliveira, L. Bilro, and R. Nogueira, *Polymer Optical Fiber Bragg Gratings : Fabrication and Sensing Applications*. Boca Raton, FL, USA: CRC Press, 2019, doi: 10.1201/9780367822705.

[21] N. G. Harbach, *Fiber Bragg Gratings in Polymer Optical Fibers*. Lausanne, Switzerland: École Polytechnique Fédérale de Lausanne, 2008.

[22] G. Statkiewicz-Barabach, D. Kowal, P. Mergo, and W. Urbanczyk, "Comparison of growth dynamics and temporal stability of Bragg gratings written in polymer fibers of different types," *J. Opt.*, vol. 17, no. 8, 2015, Art. no. 085606, doi: 10.1088/2040-8978/17/8/085606.

[23] V. I. Kopp and A. Z. Genack, "Adding twist," *Nat. Photon.*, vol. 5, no. 8, pp. 470–472, 2011, doi: 10.1038/nphoton.2011.158.

[24] N. A. Mortensen, J. R. Folkenberg, M. D. Nielsen, and K. P. Hansen, "Modal cutoff and the V parameter in photonic crystal fibers," *Opt. Lett.*, vol. 28, no. 20, pp. 1879–1881, 2003, doi: 10.1364/OL.28.001879.

[25] P. S. J. Russell, R. Beravat, and G. K. L. Wong, "Helically twisted photonic crystal fibres," *Philos. Trans. R. Soc. A Math. Phys. Eng. Sci.*, vol. 375, no. 2087, 2017, Art. no. 20150440, doi: 10.1098/rsta.2015.0440.

[26] V. Budinski and D. Donlagic, "Fiber-optic sensors for measurements of torsion, twist and rotation: A review," *Sensors*, vol. 17, no. 3, 2017, Art. no. 443, doi: 10.3390/s17030443.

[27] S. Kiesel, K. Peters, T. Hassan, and M. Kowalsky, "Behaviour of intrinsic polymer optical fibre sensor for large-strain applications," *Meas. Sci. Technol.*, vol. 18, no. 10, pp. 3144–3154, 2007, doi: 10.1088/0957-0233/18/10/S16.

[28] Z. Xiong, G. D. Peng, B. Wu, and P. L. Chu, "Highly tunable bragg gratings in single-mode polymer optical fibers," *IEEE Photon. Technol. Lett.*, vol. 11, no. 3, pp. 352–354, Mar. 1999, doi: 10.1109/68.748232.

[29] R. M. Waxler, D. Horowitz, and A. Feldman, "Optical and physical parameters of Plexiglas 55 and Lexan," *Appl. Opt.*, vol. 18, no. 1, pp. 101–104, Jan. 1979, doi: 10.1364/AO.18.000101.

[30] K. Minami, "Optical plastics," in *Handbook of Plastic Optics*. Weinheim, Germany: Wiley-VCH Verlag GmbH & KGaA, 2010, pp. 109–147, doi: 10.1002/9783527635443.

[31] MITSUBISHI RAYON CO. LTD, "General Properties of AcrypetTM," 2015.